RSC Advances

PAPER

View Article Online
View Journal | View Issue

Cite this: *RSC Adv.*, 2014, **4**, 12245

CH_x adsorption ($x = 1$–4) and thermodynamic stability on the CeO_2(111) surface: a first-principles investigation

Marco Fronzi,*[a] Simone Piccinin,[b] Bernard Delley,[c] Enrico Traversa[d] and Catherine Stampfl[e]

Received 12th February 2014
Accepted 19th February 2014

DOI: 10.1039/c4ra01224k

www.rsc.org/advances

We present an *ab initio* investigation of the interaction between methane, its dehydrogenated forms and the cerium oxide surface. In particular, the stoichiometric CeO_2(111) surface and the one with oxygen vacancies are considered. We study the geometries, energetics and electronic structures of various configurations of these molecules adsorbed on the surface in vacuum, and we extend the analysis to realistic environmental conditions. A phase diagram of the adsorbate–surface system is constructed and relevant transition phases are analyzed in detail, showing the conditions where partial oxidation of methane can occur.

I. Introduction

Solid oxide fuel cell (SOFC) technology in the recent years is receiving renewed interest due to its fuel flexibility and the high efficiency of the chemical to electrical energy conversion.[1–6] The research in this field aims to reduce the operating temperature, resulting in reduced costs, for widespread applications.[7,8] This can be achieved by the adoption of electrolytes alternative to yttria-stabilized zirconia, and by the discovery of more efficient materials for electrodes with a high and selective catalytic activity, to improve the efficiency at lower temperatures.

Cerium oxide is a good candidate as a SOFC electrolyte for operation at 950 K.[9–11] Moreover, it has been reported to be a promising anode material, in particular for direct operation with methane and other hydrocarbon fuels.[1,12,13] This is due to the ceria catalytic activity;[14–16] Its surfaces show activity with respect to several chemical reactions, in particular for the C–H bond activation of the methane molecule, proving that CeO_{2-x} acts as an active center for methane oxidation.[17] This makes it a good candidate to be used as a fuel cell anode material.[15,18]

On the other hand, methane is the main component of natural gas and there is a keen interest to understand the mechanisms of methane oxidation, used for energy production.[19] Recently, many studies have been performed in order to analyze molecule–surface interactions and surface catalytic activity of several metal oxide compounds from both an experimental and a theoretical point of view.[20,21] Direct oxidation of methane on both metal and metal-oxide surfaces has been observed, showing a very high thermodynamic efficiency limit for complete oxidation, that can reach 92%.[15,22,23] Indeed, experiments proved that methane shows chemical activity if exposed to an atmosphere containing oxygen and that a humid environment plays an important role against methane oxidation.[24–26] From this prospective, a systematic study of CH_x adsorption on cerium oxide surfaces under realistic catalytic conditions becomes crucial to gain insight into this system, with the goal of improving the efficiency of these important processes in clean energy applications.

Several theoretical computational studies have been carried out to study methane dissociation on CeO_2 under vacuum conditions.[15,27] In this paper we examine this system when in contact with two gas reservoirs, oxygen and water vapor, by means of *ab initio* atomistic thermodynamics, in order to reproduce realistic environmental conditions.[28–31] This analysis allows us to examine the effect of the composition of the atmosphere on the critical temperature for methane oxidation.

Using Density Functional Theory (DFT), in this work we provide a systematic analysis of CH_x adsorption on the stoichiometric, as well as the reduced, CeO_2(111) surface. We analyze the CH_x fragment adsorption energies in vacuum, and describe the adsorbate–surface bonds obtained by charge distribution in the adsorption process and the electronic structures of the adsorbate–surface system. The calculated adsorption and surface energies enable us to describe the trend of the Gibbs free energy under realistic catalytic conditions as a function of the chemical potential of oxygen and water. The analysis results in the construction of a surface phase diagram that shows the relative thermodynamic stability of each adsorbate–surface system; also, relevant phase transition can be analyzed in detail.

[a]*Department of Mechanical Science and Bioengineering, Graduate School of Engineering Science, Osaka University, Japan. E-mail: marco.fronzi@gmail.com*
[b]*CNR-IOM Democritos, c/o SISSA, via Bonomea 265, I-34136 Trieste, Italy*
[c]*Paul-Scherrer-Institut, CH-5232 Villigen PSI, Switzerland*
[d]*Physical Sciences and Engineering Division, King Abdullah University of Science and Technology, Kingdom of Saudi Arabia*
[e]*School of Physics, The University of Sydney, Sydney, New South Wales 2006, Australia*

II. Details of methodology

A. DFT calculations: basis set and convergence

All calculations presented in this work are performed using the generalized gradient approximation for the exchange and correlation potential due to Perdew, Burke and Erzerhof (PBE) as implemented in the all-electron DMol^3 code.[32–34] The DMol^3 method employs fast converging three-dimensional numerical integrations to calculate the matrix elements occurring in the Ritz variational method. The wave functions are expanded in terms of a double-numerical quality localized basis set with a real-space cutoff of 11 Bohr. Polarization functions and scalar-relativistic corrections are incorporated explicitly. We use (2×2) surface unit cells, and a vacuum region of ≈ 30 Å, which ensures negligible interaction between periodic replicas, and an $8 \times 8 \times 1$ k-point mesh, yielding 10 k-points in the irreducible part of the Brillouin zone.

The LDA and GGA approximations of the exchange and correlation potential are unable to properly describe the electronic structure of cerium oxide, especially in its reduced form.[35] To correct the resulting electronic structure of the reduced ceria, favouring the insulating state with respect to the metallic solution, the inclusion of the Hubbard-U term in the DFT + U approach is necessary. The choice of the value of U can be obtained either by empirically adjusting the U term, in order to reproduce the experimental spectroscopic features, or by the self-consistent linear response method.[36] However, such methodology suffers form a strong dependence of the energetics on the choice of the value of the parameter U and on the choice of the localised projectors that enter the definition of the U-dependent energy term. Yet, in several cases, this choice of U yields energy values (*e.g.* reduction energy and adsorption energies) that are significantly different from the experimental value, and an empirical adjustment of U become necessary.[35,36] As pointed out by Da Silva *et al.*, there is no unique value of U that at the same time gives a reasonable description of structural parameters, relative energies of different oxides and spectroscopic properties, hence it is not clear whether the DFT + U method provides a systematic improvement of the energetics.[35] In view of these considerations, in our study we adopt a plain DFT-GGA approach. For a more in depth discussion of the comparison between DFT + U and DFT approaches for cerium oxide surfaces we refer the reader to our earlier work on the subject.[37,38]

III. Geometries and energetics

In this section, we analyze energetics and geometries of the interaction between the CH_x (x = 1–4) and the $CeO_2(111)$ surface with and without surface oxygen vacancies, when the CH_x coverage is 0.25 mono layers (ML) under vacuum conditions. We start by considering the interaction of CH_4 with the $CeO_2(111)$ surface. Various configurations are considered for adsorption, as reported in Table 1, where the adsorption energies are calculated as follows:

$$E_{ads} = -[E_{sys} - E_{surf} - E_{mol}], \quad (1)$$

Table 1 Adsorption energies of CH_4 on different adsorption sites of the $CeO_2(111)$ surface. Namely, on top of the Ce atom, O atom, surface oxygen vacancy (V_O) and the oxygen atom located in the second layer (O_{2nd})

Config.	Adsorption energy (eV)
Ce	0.07
O	0.05
O_{2nd}	0.06
V_O	0.00

where E_{surf} is the total energy of the surface, E_{mol} that of molecule, and E_{sys} is the total energy of the surface–adsorbate system.

For the considered configurations, the methane molecule shows a weak interaction with the $CeO_2(111)$ surface and in the most favorable case, it adsorbs at the cerium site, with an adsorption energy of 0.07 eV. In this configuration, shown in Fig. 1, the methane molecule adsorbs on the surface with a hydrogen atom pointing to the surface cerium atom. The distance Ce–O in this case is 2.51 Å. This result is in line with other results in the literature, using both DFT and DFT + U approaches.[27] When an oxygen vacancy is created on the cerium oxide surface, interestingly, the interaction become repulsive. The morphology of the surface becomes therefore crucial for the first step in the methane oxidation reaction. To better analyze the nature of the interaction between CH_4 and the surface cerium atom, we studied the charge density difference (Q_d) induced by the adsorption of water on $CeO_2(111)$, defined as the difference between the charge density of the adsorbate system (Q_{s+a}) and the sum of the isolated molecule (Q_a) and the slab (Q_s), calculated as follows:

$$Q_d = Q_{s+a} - (Q_s + Q_a). \quad (2)$$

In this case, an extremely small charge redistribution is observed (therefore not reported here). The adsorption energy in the proximity of an oxygen vacancy shows a slightly repulsive interaction between methane molecule and the surface. The interaction energy, geometry and charge distribution of this system indicate a non-covalent character of the CH_4–$CeO_2(111)$

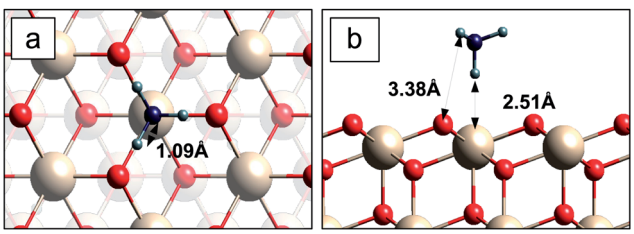

Fig. 1 Top (a) and side (b) view of adsorption sites considered for methane on the $CeO_2(111)$. (a) and (b) show methane on top of Ce atom. Large pale (gray) and small dark (red) spheres indicate Ce and O atoms, respectively. The small dark (blue) and the very small (gray) spheres represent C and H atoms respectively. Selected inter-atomic distances are indicated.

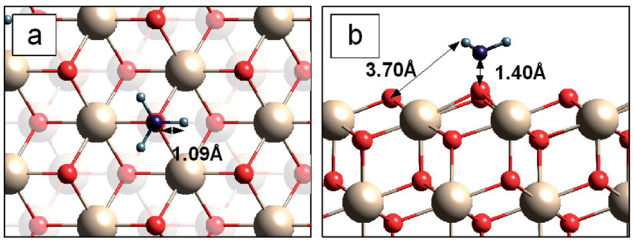

Fig. 2 Top (a) and side (b) view of adsorption sites considered for CH_3 fragment on $CeO_2(111)$. (a) and (b) show CH_3 on top of the surface O atom. The small dark (blue) and the very small (gray) spheres represent C and H atoms respectively. Selected inter-atomic distances are indicated.

bond (confirmed in the "Electronic structure" section), due the CH_4 closed shell configuration, and suggest a van der Waals nature of the interaction. DFT-GGA calculations do not include van der Waals interaction in the calculated energy, so our results include a systematic error. However, we calculate the van der Waals contribute to the interaction to be ~0.1 eV, which is relatively small if compared to the adsorption energies of the other fragments. Therefore, we can assume that our conclusions are, at least qualitatively, correct.

In order to obtain a first insight in the analysis of the CH_4 dissociation on the $CeO_2(111)$ surface, we examine the adsorption of CH_x fragments. The CH_3 fragment adsorbs on the oxygen atom site with an adsorption energy of 2.09 eV, and the distance between carbon atom and surface oxygen is 1.40 Å (see Table 2). The adsorption on the cerium atom and over the oxygen in the second layer are highly unfavored and the energy indicates a repulsive interaction. When an oxygen vacancy is created on the surface, the magnitude of the adsorption energy decreases, *i.e.* $E_{ads} = 1.80$ eV, indicating a less favorable interaction between the molecule and the reduced surface. The induced charge density of CH_3 adsorption on the $CeO_2(111)$ surface indicates a charge redistribution, as shown in Fig. 3, which shows an evident charge transfer from the surface oxygen toward the carbon. The charge accumulation is not strongly localized, however, the shared charge can be an indication of a covalent bond between the carbon atom of the fragment and the surface oxygen.

The CH_2 fragment interacts strongly with the surface, having a large adsorption energy on both the Ce and O sites (3.26 eV and 3.31 eV, respectively). Even when it adsorbs on an oxygen vacancy, the adsorption energy differs from the most stable configuration only by 9.3% of the energy bond (see Table 3). The analysis of the induced charge density indicates an evident charge transfer from the surface oxygen to the carbon atom. The shared electron charge suggests the formation of a covalent bond.

Table 2 Adsorption energies (in eV) of CH_3 on the $CeO_2(111)$ surface in different configurations. Namely, on top of the O atom and the surface oxygen vacancy (V_O)

Config.	Adsorption energy
O	2.09
V_O	1.80

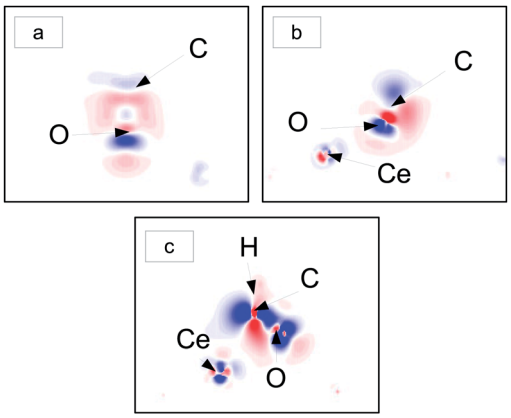

Fig. 3 Induced charge density due to the adsorption of (a) CH_3, (b) CH_2 and (c) CH on the $CeO_2(111)$ surface. The red areas indicate charge accumulation, while the blue areas indicate charge depletion.

Table 3 Adsorption energies (in eV) of CH_2 on the $CeO_2(111)$ surface in different configurations. Namely, on top of the Ce atom, O atom and surface oxygen vacancy (V_O)

Config.	Adsorption energy (eV)
Ce	3.26
O	3.31
V_O	3.00

Table 4 Adsorption energies (in eV) of CH on the $CeO_2(111)$ surface in different configurations. Namely, on top of the Ce atom, O atom and surface oxygen vacancy (V_O)

Config.	Adsorption energy (eV)
Ce	4.07
O	4.14
V_O	2.96

The last fragment analyzed in this section is CH. In this case the adsorption energy is very high when it adsorbs on both the Ce and O sites (4.07 eV and 4.14 eV, respectively) and when an oxygen vacancy is created on the surface, the interaction energy decreases to 2.96 eV, indicating a strong interaction between the oxygen vacancy and the CH fragment (Table 4). The induced charge density for the adsorption on the O site of $CeO_2(111)$ indicates an evident charge transfer. Fig. 3 shows a charge depletion around the surface oxygen and around the carbon atom in the plane cutting the aligned C, O, Ce and H atoms, and the evident charge redistribution around the cerium atom suggests a small interaction between the carbon atom and with the lower lying cerium atom.

IV. Energetics and thermodynamics

In this section we analyze the stability of the surfaces under the realistic environmental conditions of a humid atmosphere

(H_2O) containing pure oxygen gas. Each adsorbate–surface system, previously considered in a vacuum space, is now analyzed when in thermodynamic equilibrium with two independent reservoirs of oxygen gas and water in its vapor phase. We take into consideration the situation where the $CeO_2(111)$ surface has one of the CH_x fragment adsorbed, and where the oxygen and water chemical potentials can hypothetically vary independently of each other within two extreme limits of poor and rich concentration. This approach allows us to calculate the energy of each surface–molecule system under every possible value of oxygen/water partial pressure. The surface free energy for each of the surface–molecule systems is calculated as follows:

$$\gamma(\{p_i\}, T) = \frac{1}{2A}\left[G - \sum N_i \mu_i(p_i, T)\right], \quad (3)$$

where G is the Gibbs free energy of the solid with surface area A (the factor $\frac{1}{2}$ is due to the presence of two identical surfaces, one on each side of the slab); $\mu(p_i, T)$ is the chemical potential of the species i that depends on pressure and temperature of the system, and N_i is the number of atoms of component i of the system.

The chemical potentials, $\mu(p, T)$, of oxygen and water vapor depend on temperature and pressure according to:

$$\mu_O(p, T) = \frac{1}{2}\left[E_{O_2} + \tilde{\mu}_{O_2}(p^0, T) + k_B T \ln\left(\frac{p_{O_2}}{p^0}\right)\right] \quad (4)$$

and

$$\mu_{H_2O}(p, T) = E_{H_2O} + \tilde{\mu}_{H_2O}(p^0, T) + k_B T \ln\left(\frac{p_{H_2O}}{p^0}\right) \quad (5)$$

In Fig. 6 these quantities are re-defined in order to have 0 eV as oxygen and water rich-limiting conditions, and the plot is constructed as a function of $\Delta\mu_O$ and $\Delta\mu_{H_2O}$. The rich and poor limit for the chemical potential can be calculated considering oxygen and water to be in thermal equilibrium with the $CeO_2(111)$ surface. The oxygen-poor limit corresponds to the condition when CeO_2 dissociates into Ce and O_2, while the oxygen-rich limit corresponds to the condition when oxygen molecules condense on the surface. Analogous considerations apply for the water, where an additional restriction has to be applied for the water-rich limit by considering water staying in the gas phase at any temperature or pressure. For this specific system, the poor-limit conditions for the chemical potentials are $0 > \Delta\mu_O > -5.01$ eV and $\Delta\mu_{H_2O} < -0.91$ eV. A more detailed description of the derivation of these quantities can be found elsewhere.[38]

Eqn (3) describes the surface free energy, γ, for each of the surface–molecule systems, *i.e.* a function of the two variables $\Delta\mu_O$ and $\Delta\mu_{H_2O}$. For each value of $\Delta\mu_O$ and $\Delta\mu_{H_2O}$, the value of γ with lower energy is the most thermodynamically stable. Fig. 6 is obtained by projecting the surface with the lowest free energy on the $\Delta\mu_O - \Delta\mu_{H_2O}$ planes so that each colored area represents the most stable surface–molecule system for given values of the chemical potential of oxygen and water. In addition to the surfaces analyzed in the previous section, we include in Fig. 6 an additional surface, with the label "$CeO_2 + V_O + OH–H–CH_4$", which represents the adsorbed CH_4 on the reduced $CeO_2(111)$ at environmental conditions that induce the surface to be hydrolyzed due to water dissociation. This surface energy has been calculated by correcting the hydrolyzed $CeO_2(111) + V_O$ surface energy calculated in our previous work, with the adsorption energy of the CH_4 calculated here.[38]

In Fig. 6, the plot can be divided into two main areas: one including the blue, the red, and the white ones where CH_4 is stable on the reduced and stoichiometric surfaces, respectively, and the rest of them where the CH_4 is not stable. In these other areas CH_x fragments are stable, indicating the environmental conditions where CH_4 will dissociate on the $CeO_2(111)$ surface. As a general trend, for each fixed value of $\Delta\mu_O$ the partial pressure of the water plays an important role in the dehydrogenation process. In this case, the loss of one or more hydrogen atoms, and therefore the loss of one or more electrons by the methane molecule, is equivalent to an oxidation process.

Having defined the relative stability of each system, we now can consider under which conditions relevant transition phases occur. Fixing the chemical potential of water imposing a water-rich condition ($\Delta\mu_{H_2O} = -0.91$ eV), for an atmospheric pressure $p = 1$ atm, we find the surface to be hydrolyzed when the temperature is above $T_c \sim 1100$ K, while no surface reduction occurs. To find a reduced surface, the value of the chemical potential of water has to decrease to $\Delta\mu_{H_2O} \sim -2.1$ eV. Under this conditions, for an atmospheric pressure $p = 1$ atm, we find the surface to be reduced when the temperature is above $T_c \sim 1200$ K while for $p = 10^{-14}$ atm the surface is reduced at temperature around $T_c \sim 500$ K, indicating that the pressure of the oxygen and water play a fundamental role in changing the critical temperature for surface reduction.

Under atmospheric conditions, we can consider the partial pressure of the water vapor and oxygen to be around 1 atm. Once both values are fixed, we can move on the phase diagram by varying the temperature of both gas reservoirs, drawing a curve on the phase diagram in Fig. 6. This isobar line starts at 300 K in the CeO_2–CH_4 phase and crosses into the CeO_2–CH_3 and CeO_2–CH_3 phases upon increasing the temperature. The resulting transition temperature between $CeO_2 + CH_4$ and $CeO_2 + CH_3$ is $T \sim 750$ K, while between $CeO_2 + CH_3$ and $CeO_2 + CH$ it is $T \sim 1050$ K. This result suggests that a temperature above $T_c = 750$ K in the atmosphere is a sufficient condition for the partial oxidation of methane on the $CeO_2(111)$ surface, which is in a good agreement with Haneda *et al.*, who confirmed CeO_2 to show catalytic activity for methane oxidation at 673 K.[17] The difference could be due to the presence, supposedly small, of other facets rather than the more stable (111) in the specimen.

As shown in Fig. 6, there is a competing mechanism played by oxygen and water chemical potentials against methane dissociation. If we let the two chemical potentials to be independent, for a given T on a generic isobar curve, an increment of the $\Delta\mu_{H_2O}$ only, would result in a higher critical temperature for CH_4 oxidation, while a change of $\Delta\mu_O$ would have the opposite effect. This result qualitatively confirms the effect of water on methane oxidation observed experimentally on several other materials.[24,25]

In this work we do not consider activation barriers since we are focusing on an analysis of the thermodynamics of the process to investigate the relative stability of the intermediate states. However, under the conditions of pressure and temperature considered, the system can be considered to be in thermodynamic equilibrium.

V. Electronic structure

In this section, we analyze the electronic structures of the most stable surfaces identified in the previous section (Fig. 1, 2, 4 and 5).

Fig. 7(a) shows the projected density-of-states (pDOS) for a stoichiometric surface with an adsorbed methane molecule. There is no evidence of hybridization in the states of the carbon atom of the methane molecule and the nearest surface atoms. When focusing on the surface atoms, we observe that the CeO_2(111) pDOS exhibits a strong localization of the Ce-4f band, typical of strongly correlated materials, centered at 1 eV, while the Ce-5d states are delocalized in the range of 5 to 10 eV. The highest occupied band is mainly derived from the 2p state of oxygen, which has an overlap in energy with the Ce-4f and Ce-5d states in the range −5 eV to −1 eV. The C_{CH_4}-2p peaks preserve their narrow profile, indicating a molecular-like behavior and confirming a non-covalent (van der Waals) nature of the interaction.

For the case of CH_3 chemisorbed on CeO_2(111) (see Fig. 7(b)), the C_{CH_3}-2p peaks shift toward lower energies by 2 eV. The

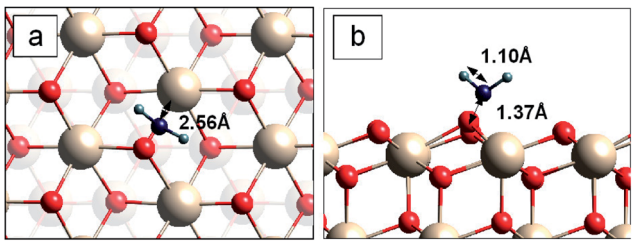

Fig. 4 Top (a) and side (b) view of adsorption sites considered for CH_2 on the CeO_2(111). (a) and (b) show CH_2 adsorbed on top of the O atom. Large pale (gray) and small dark (red) spheres indicate Ce and O atoms, respectively. The small dark (blue) and the very small (gray) spheres represent C and H atoms respectively. Selected inter-atomic distances are indicated.

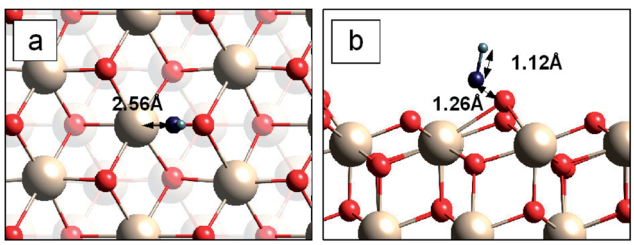

Fig. 5 Top (a) and side (b) view of adsorption sites considered for CH on CeO_2(111). (a) and (b) show CH adsorbed at a surface O atom. Large pale (gray) and small dark (red) spheres indicate Ce and O atoms, respectively. The small dark (blue) and the very small (gray) spheres represent C and H atoms respectively. Selected inter-atomic distances are indicated.

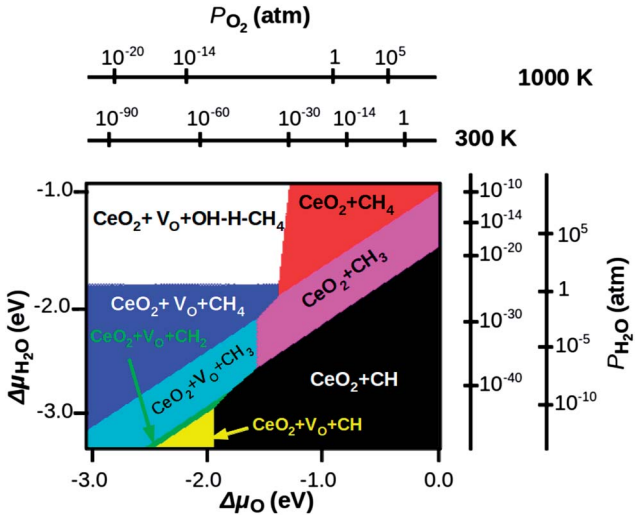

Fig. 6 Surface phase diagram of stable structures of CeO_2(111) + CH_x in equilibrium with a humid environment, as a function of $\Delta\mu_O$ and $\Delta\mu_{H_2O}$ in the gas phase. The additional axes show the corresponding pressure scales at $T = 300$ and 1000 K.

O_{CeO_2}-2p shows a splitting in two narrow peaks and there is an evident overlapping between C_{CH_3}-2p and O_{CeO_2}-2p at around −7 eV, indicating an evident surface–molecule interaction. This behavior is typical of atomic-like orbitals interacting with a narrow band, in this specific case the peak of O_{CeO_2}-2p.[39] In this case, the CeO_2(111) surface shows a metallic behavior. However, the occupation of the 4f band is very low, and the energy of the surface can be considered indistinguishable to the semi-conducting surface.

When CH_2 adsorbs on the surface (see Fig. 7(c)), the hybridization of the orbitals is more evident. The O_{CeO_2}-2p band shows a further shift to −6 eV and a broadening of one of the peaks. There is also an evident overlapping of O_{CeO_2}-2p, O_{CH_2}-2p and H_{CH2}-2p at around −8 eV and −4 eV, indicating a strong interaction.

When the fragment CH is adsorbed on the surface (see Fig. 7(d)), the narrow peak of the C_{CeO_2}-2p exhibits a broadening, typical of atomic-like orbitals interacting with a broad band.[39] This feature suggests chemisorption of the adsorbate on the surface, consistent with the value of the adsorption energy previously shown. Also, in the adsorption of the CH fragment, the surface exhibits a metallic behavior. However, analogous considerations on the energy of the system can be done as in the case of the CH_3 adsorption.

VI. Summary and conclusions

We performed DFT calculations in order to gain insight into the structure and energetics of CH_x adsorption on the stoichiometric and reduced CeO_2(111) surface for a coverage of 0.25 ML. Our results show that, on the stoichiometric surface, the most stable structure is the one in which methane is adsorbed on Ce. However, the adsorption energy indicates a very weak interaction. Also, we found that surface oxygen vacancies do not increase the strength of the interaction, and that adsorption

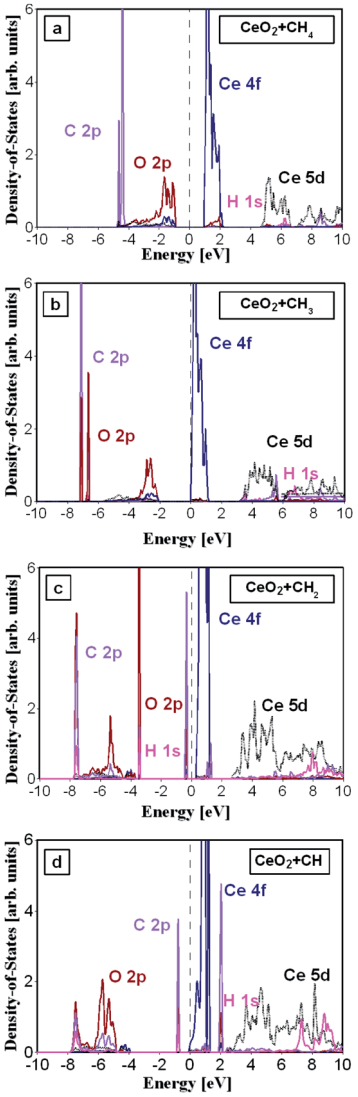

Fig. 7 Projected density-of-states of CH_x adsorbed on CeO_2(111). (a)–(d) represents the CH_4, CH_3, CH_2 and CH on the CeO_2(111) surface. The black and the solid dark gray (blue) lines represent, respectively, the 5d and the 4f states of the cerium atoms, while the gray (red) line represents the 2p state of the oxygen atoms. The pale gray (magenta and purple) lines represent, respectively, the hydrogen 1s and carbon 2p of the CH_x fragment. The vertical dashed line represents the Fermi energy.

energies become stronger when methane is dehydrogenated. From the surface phase diagram, constructed by employing the *ab initio* constrained thermodynamics approach, we studied the relevant phase transitions. Fixing the chemical potential of water and imposing a water-rich condition, when the pressure of the atmosphere is $p = 1$ atm, the hydrolyzed CeO_2(111) surface is thermodynamically stable for values of temperature above $T_c \sim 1100$ K, and no surface reduction occur. When the value of the chemical potential of water has to decrease to $\Delta\mu_{H_2O} \sim -2.1$ eV, for an atmospheric pressure $p = 1$ atm, we find the surface to be reduced when the temperature is above $T_c \sim 1200$ K while for $p = 10^{-14}$ atm the surface is reduced at temperature around $T_c \sim 500$ K, indicating the fundamental role of the oxygen and water in determining the critical temperature for the reduction of the surface. Also, we estimated the sufficient conditions to obtain partial oxidation of the methane to be, considering the partial pressure of both water vapor and oxygen gas at 1 atm, $T_c \sim 750$ K, in good agreement with experimental results. A competing mechanism played by oxygen and water chemical potentials against methane dissociation was found, and while an increment of $\Delta\mu_{H_2O}$ would result in a higher critical temperature for CH_4 oxidation, a change of $\Delta\mu_O$ would have the opposite effect. This result qualitatively confirms the effect of water on methane oxidation observed experimentally on several other material surfaces.

Acknowledgements

The authors gratefully acknowledge support from the Australian Research Council (ARC), the Australian National Computational Infrastructure (NCI) and the Australian Center for Advanced Computing and Communication (AC3). MF expresses his gratitude to Jason Gao and Irina Holca for proofreading the manuscript.

References

1 E. P. Murray, T. Tsai and S. A. Barnett, *Nature*, 1999, **400**, 649.
2 N. V. Long, Y. Yang, C. M. Thi, N. V. Minh, Y. Cao and M. M. Nogami, *Nano Energy*, 2013, **2**, 636.
3 E. Kendrick and P. R. Slater, *Annu. Rep. Prog. Chem., Sect. A: Inorg. Chem.*, 2013, **109**, 139.
4 S. McIntosh and R. J. Gorte, *Chem. Rev.*, 2004, **104**, 4845.
5 N. H. Menzler, F. Tietz, S. Uhlenbruck, H. P. Buchkremer and D. Stoever, *J. Mater. Sci.*, 2010, **45**, 3109.
6 E. D. Wachsman, C. A. Marlowe and K. T. Lee, *Energy Environ. Sci.*, 2010, **5**, 5498.
7 E. D. Wachsman and K. T. Lee, *Science*, 2011, **334**, 935.
8 E. Fabbri, L. Bi, D. Pergolesi and E. Traversa, *Adv. Mater. Sci.*, 2012, **24**, 195.
9 B. C. H. Steele, *Solid State Ionics*, 2000, **95**, 129.
10 V. Esposito and E. Traversa, *J. Am. Ceram. Soc.*, 2008, **91**, 1037.
11 D. P. J. S. Ahn, M. A. Camaratta, H. Yoon, B. W. Lee, K. T. Lee, D. W. Jung, E. Traversa and E. D. Wachsman, *Electrochem. Commun.*, 2009, **11**, 1504.
12 S. D. Park, J. M. Vohs and R. J. Gorte, *Nature*, 2000, **404**, 265.
13 T. H. Shin, S. Ida and T. Ishihara, *J. Am. Chem. Soc.*, 2011, **133**, 19399.
14 A. Trovarelli, *Catal. Rev.: Sci. Eng.*, 1996, **38**, 439.
15 D. Knapp and T. Ziegler, *J. Phys. Chem. C*, 2008, **112**, 17311.
16 M. Cargnello, J. J. D. Jaen, J. C. H. Garrido, K. Bakhmutsky, T. Montini, J. J. C. Gamez, R. J. Gorte and P. Fornasiero, *Science*, 2012, **337**, 713.
17 M. Haneda, T. Mizushima and N. Kakuta, *J. Phys. Chem. B*, 1998, **102**, 6579.
18 N. Laosiripojana, S. Assabumrungrat and S. Charojrochkul, *The Joint International Conference on Sustainable Energy and Environment*, 2004.

19 R. J. Farrauto, *Science*, 2012, **337**, 659.
20 P. S. Moussounda, M. F. Haroun, G. Rakotovelo and P. Légaré, *Surf. Sci.*, 2007, **601**, 3697.
21 B. Monnerat, L. Kiwi-Minsker and A. Renken, *Chem. Eng. Sci.*, 2001, **56**, 633.
22 E. Odier, Y. Schuurman and C. Mirodatos, *Catal. Today*, 2007, **127**, 230.
23 S. Bharadwaj and L. Schmidt, *Fuel Process. Technol.*, 1995, **42**, 109.
24 C. F. Cullis and B. M. Willatt, *J. Catal.*, 1984, **86**, 187.
25 F. H. Ribeiro, M. Chow and R. A. Dallabetta, *J. Catal.*, 1994, **146**, 537.
26 R. Kikuchi, S. Maeda, K. Sasaki, S. Wennerströmc and K. Eguchi, *Appl. Catal., A*, 2002, **232**, 23.
27 A. D. Mayernick and M. J. Janik, *J. Phys. Chem. C*, 2008, **112**, 14955.
28 C. Stampfl, *Catal. Today*, 2005, **105**, 17.
29 K. Reuter and M. Scheffler, *Phys. Rev. B: Condens. Matter Mater. Phys.*, 2002, **65**, 035406.
30 K. Reuter and M. Scheffler, *Phys. Rev. B: Condens. Matter Mater. Phys.*, 2003, **68**, 045407.
31 C. Stampfl, M. V. Ganduglia-Pirovano, K. Reuter and M. Scheffler, *Surf. Sci.*, 2002, **500**, 368.
32 J. P. Perdew, K. Burke and M. Erzerhof, *Phys. Rev. Lett.*, 1996, **77**, 3865.
33 B. Delley, *J. Chem. Phys.*, 1990, **92**, 508.
34 B. Delley, *J. Chem. Phys.*, 2000, **113**, 7756.
35 J. L. F. Da Silva, M. V. Ganduglia-Pirovano and J. Sauer, *Phys. Rev. B: Condens. Matter Mater. Phys.*, 2007, **75**, 045121.
36 M. Cococcioni and S. De Gironcoli, *Phys. Rev. B: Condens. Matter Mater. Phys.*, 2005, **71**, 035105.
37 M. Fronzi, A. Soon, B. Delley, E. Traversa and C. Stampfl, *J. Chem. Phys.*, 2009, **131**, 104701.
38 M. Fronzi, S. Piccinin, B. Delley, E. Traversa and C. Stampfl, *Phys. Chem. Chem. Phys.*, 2009, **11**, 91889199.
39 J. K. Nørskov, *Rep. Prog. Phys.*, 1990, **53**, 1253.